Segmenting Atrial Fibrosis from Late Gadolinium-Enhanced Cardiac MRI by Deep-Learned Features with Stacked Sparse Auto-Encoders

Guang Yang [*1,2], Xiahai Zhuang [*3], Habib Khan [1,2], Shouvik Haldar [1], Eva Nyktari [1], Xujiong Ye [4], Greg Slabaugh [5], Tom Wong [1], Raad Mohiaddin [1,2], Jennifer Keegan [1,2], David Firmin [1,2]

[1] Cardiovascular Biomedical Research Unit, Royal Brompton Hospital, SW3 6NP, London, UK
[2] National Heart and Lung Institute, Imperial College London, SW7 2AZ, London, UK
[3] School of Data Science, Fudan University, Shanghai, 201203, China
[4] School of Computer Science, University of Lincoln, LN6 7TS, Lincoln, UK
[5] Department of Computer Science, City University London, EC1V 0HB, London, UK
[*] Corresponding authors: GY—g.yang@imperial.ac.uk and XZ— zxh@fudan.edu.cn

Abstract. The late gadolinium-enhanced (LGE) MRI technique is a well-validated method for fibrosis detection in the myocardium. With this technique, the altered wash-in and wash-out contrast agent kinetics in fibrotic and healthy myocardium results in scar tissue being seen with high or enhanced signal relative to normal tissue which is 'nulled'. Recently, great progress on LGE MRI has resulted in improved visualization of fibrosis in the left atrium (LA). This provides valuable information for treatment planning, image-based procedure guidance and clinical management in patients with atrial fibrillation (AF). Nevertheless, precise and objective atrial fibrosis segmentation (AFS) is required for accurate assessment of AF patients using LGE MRI. This is a very challenging task, not only because of the limited quality and resolution of the LGE MRI images acquired in AF but also due to the thinner wall and unpredictable morphology of the LA. Accurate and reliable segmentation of the anatomical structure of the LA myocardium is a prerequisite for accurate AFS. Most current studies rely on manual segmentation of the anatomical structures, which is very labor-intensive and subject to inter- and intra-observer variability. The subsequent AFS is normally based on unsupervised learning methods, e.g., using thresholding, histogram analysis, clustering and graph-cut based approaches, which have variable accuracy. In this study, we present a fully-automated multi-atlas propagation based whole heart segmentation method to derive the anatomical structure of the LA myocardium and pulmonary veins. This is followed by a supervised deep learning method for AFS. Twenty clinical LGE MRI scans from longstanding persistent AF patients were entered into this study retrospectively. We have demonstrated that our fully automatic method can achieve accurate and reliable AFS compared to manual delineated ground truth.

1 Introduction

Atrial fibrillation (AF) is the most commonly observed cardiac arrhythmia that occurs in up to 2% of the general population with increased prevalence in the aged pop-

adfa, p. 1, 2011.

ulation [1]. AF can cause substantial morbidity and mortality; for example, it is associated with a five-fold incidence of stroke, three-fold risk of congestive heart failure and doubles the possibility of dementia that has a major worldwide public health impact [2]. Currently, the pathophysiology of AF is not fully understood; however, previous studies on both animal and human experimental models have shown that multiple disease pathways, e.g., structural, contractile, or electrical alterations, can promote abnormal electrical impulse formation and propagation [3]. Fibrosis in the left atrium (LA) is the hallmark of atrial structural remodeling, and is one of the major risk factors for AF progression [4, 5]. Moreover, studies have shown that ectopic beats from the pulmonary veins (PVs) can frequently trigger the AF [6]. Based on these findings, minimally invasive radio-frequency catheter ablation (CA) using the pulmonary vein antrum isolation method has been developed as a front-line therapy for symptomatic AF patients refractory to drug treatment [7], but suffers a >30% recurrence rate [8].

In order to understand AF and facilitate better management and prognosis, techniques have been developed to evaluate the LA wall composition and assess the circumferential PVs scarring that results from CA. Currently, the electro-anatomical mapping (EAM) system is used as a clinical reference standard technique for the assessment of extent and distribution of native atrial fibrosis and post-ablation scar. This is normally performed during an electrophysiological procedure and has the major drawback of invasiveness and suboptimal accuracy, which has been reported as being up to 10 mm in the localization of atrial fibrosis [9, 10]. Moreover, there are the potentially hazardous effects of ionizing radiation for the patients using EAM.

In contrast, the late gadolinium-enhanced (LGE) MRI, which is noninvasive and without ionizing radiation, allows the detection and quantification of native fibrosis and post-ablation scars by highlighting the slow washout kinetics of the gadolinium in these tissues [11–15]. Firstly, the extent and distribution of native fibrosis identified in the pre-ablation baseline LGE MRI scan has emerged as the strongest independent predictor of AF recurrence after the first ablation [13]. Secondly, LGE MRI can be used as a powerful tool to detect ablation-induced fibrosis formed by radiofrequency energy delivered in the atrial myocardium [11]. This has a potential role in recognizing ablation line gaps, which are the main reason of ablation failure [11, 16]. In addition, LGE MRI can be also useful to guide the ablation procedure [11, 17].

Despite the excellent results of using LGE MRI in the assessment of ventricular fibrosis and its promising potential in the detection of atrial scars, there are still challenges to be addressed when applying LGE MRI for AF patients in clinical practice: (1) frequently the image quality of pre-ablation LGE MRI scans is poor due to residual respiratory motion, heart rate variability, low signal-to-noise ratio (SNR), and gadolinium wash-out during the long acquisition (current scanning time is around 6–10 minutes per patient); (2) the resolution of LGE MRI images is limited compared to the thinness (about 3 mm) of the LA wall; (3) the various morphologies of the LA wall and PVs anatomy; and (4) confounded enhancement from surrounding heart substructures, e.g., blood, aorta, spine, and esophagus. These can result in poor delineation of the LA myocardium and cause a large number of false positives in the atrial fibrosis delineation.

Essentially, there are two main steps required to analyze fibrotic tissues from LGE MRI images: (1) segmentation of the anatomical structure of the LA and PVs and (2) the atrial fibrosis segmentation (AFS).

For the segmentation of the anatomical structure of the LA and PVs, most previous studies have relied on manual delineation [7, 13, 18, 19], which potentially suffers from large inter- and intra-observer variability and is also very time-consuming. Semi-automatic and automatic methods have been proposed to solve this task, e.g., using thresholding with region growing [20], statistical shape model [21] and atlas propagation [22] based approaches. However, these methods required further operator's manual intervention [20, 21] or used un-gated first-pass MR angiography (MRA) data [22], which may cause difficulties in co-registration with the respiratory and cardiac gated LGE MRI data.

For the AFS, to the best of our knowledge, most studies applied unsupervised learning based methods, e.g., using histogram analysis [13], k-means clustering [18] and graph-cut [21] based approaches. In addition, maximum intensity projection (MIP) can provide intuitive visualization of the atrial fibrosis [11, 12, 20, 22]; however, this is only a visualization technique for hyper-enhancement regions, rather than a segmentation method that can result in volumetric quantification [21]. Recently, a grand challenge was carried out to benchmark different algorithms for solving AFS [19] including 8 submissions for the competition. These benchmarked algorithms were all unsupervised learning based methods [19]. The challenge included data acquired from multiple institutions, and the LA endocardium and cavity for each scan were provided to all the participants beforehand. Promising results were achieved for the best performing algorithms. However, there were large variances in the performances especially for the pre-ablation cases, which may be attributed to the fact that the image quality was generally worse and the native fibrosis is more diffuse. Therefore, the challenge of atrial fibrosis segmentation and assessment remains open. Moreover, the inaccurate AFS could be one of the major reasons for poor reproducibility of the correlation between atrial fibrosis identified by LGE MRI (enhanced regions) and EAM (low voltage regions) [23], [24].

In this study, we present a fully automatic framework for an efficient and objective atrial fibrosis assessment using: (1) a fully-automated multi-atlas based whole heart segmentation (MA-WHS) method to solve the LA and PVs anatomy and (2) a fully automatic supervised deep learning method for the AFS. Compared with the ground truth formed by manual delineation, our fully automatic framework obtains promising segmentation results, which are comparable to other state-of-the-art methods.

2 Method

2.1 Cardiac MRI Data Acquisition

Cardiac MRI acquisitions were performed on a Siemens Magnetom Avanto 1.5T scanner. Transverse navigator-gated 3D LGE MRI [11, 13, 25] was performed using an inversion prepared segmented gradient echo sequence (TE/TR 2.2ms/5.2ms) 15

minutes after gadolinium (Gd) administration when a transient steady-state of Gd wash-in and wash-out of normal myocardium had been reached [26]. LGE MRI images were scanned with a field-of-view 380×380mm^2 and reconstructed to 60–68 slices at 0.75×0.75×2mm^3.

In the LGE MRI images, healthy myocardium is 'nulled' and only fibrotic tissues are seen with high signal; therefore, it is hard to extract the anatomical structure of the LA and PVs directly from LGE MRI images. Instead of using un-gated MRA as previous studies described, in our study, a respiratory and cardiac gated 3D Roadmap image, which is acquired using a balanced steady state free precession sequence (TE/TR 1ms/2.3ms), has been scanned for each patient to derive the anatomical structure of the LA and PVs. Our roadmap data were acquired with a field-of-view 380×380mm^2 and reconstructed to 160 slices at 0.8×0.8×1.6mm^3.

Both 3D LGE MRI and Roadmap data were acquired during free-breathing using a crossed-pairs navigator positioned over the dome of the right hemi-diaphragm with a navigator acceptance window size of 5mm and continuously adaptive windowing strategy based respiratory motion control [27].

2.2 Patients

Cardiac MRI was performed in longstanding persistent AF patients between 2011–2013 in agreement with the local regional ethics committee. A Likert-type scale was applied to score the image quality of each LGE MRI scan, e.g., 0 (non-diagnostic), 1 (poor), 2 (fair), 3 (good) and 4 (very good) depending on the level of SNR, appropriate inversion time, and the existence of navigator beam and ghost artifacts.

Ten pre-ablation scans with image quality ≥2 have been retrospectively entered into this study (~60% of all the scanned pre-ablation cases). To make a balanced dataset, we randomly selected 10 post-ablation cases from all the 26 post-ablation scans with image quality ≥2 (~92% of all the scanned post-ablation cases).

2.3 Anatomical Structure Delineation for the LA and PVs

In this study, we applied a MA-WHS method to segment the anatomical structure of the LA and PVs [28]. This has been done on the Roadmap images and then mapped to LGE MRI. Our segmentation consists of two major steps: (1) atlas propagation based on image registration algorithms and (2) label fusion from multi-atlas propagated segmentation results as described in [28].

The whole heart atlases were constructed using 30 MRI Roadmap studies retrieved from the Left Atrium Segmentation Grand Challenge organized by King's College London [29]. For each atlas dataset, we have manual labels of all the heart substructures including the right and left ventricles, the right and left atria, the aorta, the pulmonary artery, the pulmonary veins and the appendages. MA-WHS executes the atlas-to-target registration for each atlas dataset ($\boldsymbol{A}_a, \boldsymbol{L}_a | a = 1, \dots N$), where $\boldsymbol{A}_\mathrm{a}$ and $\boldsymbol{L}_\mathrm{a}$ are the intensity image and the corresponding segmentation label image of the a-th atlas ($N = 30$). Then a set of warped atlases can be derived $\{(A_a, L_a) | a = 1, \dots N\}$ for label fusion, which is achieved using local weighted and multi-scale based label

fusion (MSP-LF),

$$L_I(x) = \underset{l \in \{l_{bk}, l_{la}\}}{\operatorname{argmax}} \sum_a w_a(S(I, A_a, x))\delta(L_a(x), l) \quad (1)$$

where l_{bk} and l_{la} are the labels of the background and LA and PVs, respectively, and the local weight $w_a(\cdot) \propto S(\cdot)$ is determined by the local similarity $S(\cdot)$ between the target image and the atlas. $\delta(p, q)$ is the Kronecker delta function which returns 1 when $p = q$ and returns 0 otherwise.

In MSP-LF, the local similarity of patches using a multi-scale strategy is computed as follows,

$$S_{\text{msp}}(I, A_a, x) = \sum_s S\left(I^{(s)}, A_a^{(s)}, x\right), \quad (2)$$

in which $I^{(s)} = I * \text{Gaussian}(0, \sigma_s)$ is the target image from s scale-space that is computed from the convolution of the target image with Gaussian kernel function with scale s. Here, we computed the local similarity in multi-scale images using the conditional probability of the images, that is

$$S\left(I^{(s)}, A_a^{(s)}, x\right) = p(i_x|j_x) = \frac{p(i_x, j_x)}{p(j_x)} \quad (3)$$

where $i_x = I^{(s)}(x)$ and $j_x = A_a^{(s)}(x)$ and the conditional image probability is obtained from the joint and marginal image probability which can be calculated using the Parzen window estimation [30].

For each patient case, the Roadmap dataset was then registered to the LGE MRI dataset using the DICOM header data, and then refined by affine and nonrigid registration steps. The resulting transformation was applied to the MA-WHS derived cardiac anatomy to segment the anatomical structure of the LA and PVs on the LGE MRI dataset.

In this study, we validated the anatomical structure segmentation against established ground truth from manual segmentations by experienced expert cardiologists specialized in cardiac MRI. We evaluated the segmentation accuracy using Dice score [31], Hausdorff distance (HD) [32] and Average Surface Distance (ASD) [31].

2.4 Training Datasets and Ground Truth Construction for AFS

The fixed-size window or regular pixel-grid is a traditional way to select patches from larger images prior to feature extraction [33], and has been widely used in deep convolutional neural networks based classification. In this study, we used a Simple Linear Iterative Clustering (SLIC) [34] based method to partition pixels into meaningful 'atomic' regions, i.e., super-pixels (SPs), based on certain similarity metrics (Fig. 1 (c)). In addition, SLIC based over-segmentation can be more consistent with the object boundaries in the image and is able to avoid producing outputs with zigzag boundaries that can be normally observed using relatively large sliding windows [33].

In order to create training datasets for our further supervised learning based AFS, we asked experienced cardiologists specialized in cardiac MRI to perform manual mouse clicks on the LGE MRI images to label the enhanced atrial fibrotic regions (Fig. 1 (b)). These manual mouse clicks were done on the original LGE MRI images

without the SPs grid overlaid, as this would reduce the visibility of the enhancement on LGE MRI images. The coordinates of the mouse clicks were used to select the enhanced SPs. Only one mouse click is taken into account if multiple clicks dwell in the same super-pixel.

As aforementioned, the anatomical structure of the LA and PVs was segmented using a MA-WHS method. Then a morphological dilation was applied (assuming the LA wall thickness is 3mm) to extract the LA wall and PVs. The blood pool regions were derived by another morphological erosion (5mm) from the endocardial LA boundary and the pixel intensities throughout the image were normalized according to the blood pool intensities [19]. We masked the selected enhanced SPs using the LA wall and PVs segmentation. Only the SPs having a defined overlap (≥20%) with the LA wall and PVs segmentation were selected as enhancement (these enhanced SPs were then labeled as 1). Other enhanced SPs were discarded as they were considered to be enhancement from other confounded tissues. As seen in (Fig. 1 (e)), the other SPs overlapped with the LA wall and PVs but not selected as enhancement were considered as unenhanced (these unenhanced SPs were then labeled as 0).

Once we extracted the enhanced SPs, they were combined to create a binary image, i.e., 1 for enhanced SPs and 0 for unenhanced. The binary image was overlaid on the original LGE MRI images and our cardiologists performed manual corrections to create the final boundaries (ground truths) for the enhanced atrial fibrosis.

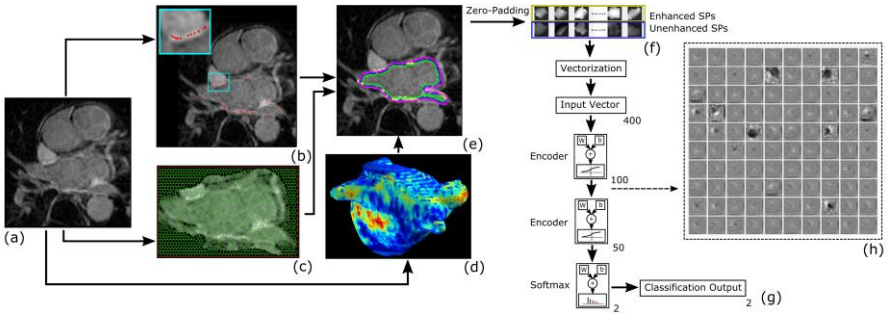

Fig. 1. (a) Original LGE MRI image of a post-ablation example case; (b) Manual mouse clicks performed by cardiologists to identify enhanced fibrotic tissues; (c) SLIC over-segmentation of the original LGE MRI image (only a ROI of the LA region shown); (d) 3D rendering of the MA-WHS results with 3D MIP based visualization of the enhanced fibrotic tissues; (e) Labeled enhanced (yellow) and unenhanced (blue) SPs that will be used to train our classification model; (f) Zero-padded SP patches (yellow box: enhanced SPs and blue box: unenhanced SPs); (g) SSAE based classification; (h) Visualization of the weights derived from the first auto-encoder.

2.5 Deep Learning via Stacked Sparse Auto-Encoders for AFS

After we obtained the over-segmented SPs, the Stacked Sparse Auto-Encoders (SSAE) [35] were initially pre-trained in an unsupervised manner without using the labels of the SPs. An auto-encoder neural network tries to learn an approximation to the identity function to replicate its input at its output using a back-propagation algorithm, that is $\hat{\mathrm{X}} = h_{\mathrm{W,b}}(\mathrm{X}) \approx \mathrm{X}$, in which $\mathrm{X} = \{x_1, x_2, \ldots, x_m\}, \mathrm{X} \in \Re^{n \times m}$ is a matrix

storing all the input training vectors $x_i \in \Re^n$. Each input vector x_i was formed by: (1) zero-padding all the SPs into a 20×20 matrix, which is the smallest bounding box for the largest super-pixel dimensions (Fig. 1 (f)), and (2) vectorizing the 20×20 matrix into a 400×1 vector. The cost function of this pre-training can be written as

$$\arg\min_{\mathrm{W}^l} J_a(\mathrm{W}^l) = \frac{1}{2m}\sum_{i=1}^{m}\|\hat{x}_i - x_i\|_2^2 + \frac{\lambda}{2}\|\mathrm{W}^l\|_2^2 + \beta\sum_{j=1}^{k}\mathrm{KL}(\rho||\hat{\rho}_j) \qquad (4)$$

where m is the number of input training vectors, k is the number of hidden nodes, λ is the coefficient for the L_2 regularization term, β is the weight of sparsity penalty, KL is the Kullback-Leibler divergence function $\mathrm{KL}(\rho||\hat{\rho}_j) = \rho\log\frac{\rho}{\hat{\rho}_j} + (1-\rho)\log\frac{1-\rho}{1-\hat{\rho}_j}$, ρ is sparsity parameter that specifies the desired level of sparsity, $\hat{\rho}_j$ is probability of firing activity that is $\hat{\rho}_j = \frac{1}{m}\sum_{i=1}^{m} h_j(x_i)$. The unsupervised pre-training is performed one layer at a time by minimizing the error in reconstructing its input and learning an encoder and a decoder, which yields an optimal set of weights W and biases b stored in W^l. If the number of hidden nodes k is less than the number of visible input nodes n, then the network is forced to learn a compressed and sparse representation of the input [35] (Fig. 1 (g) and (h)).

Second, a Softmax layer was added as the activity classification model $h_\theta(x_i)$ to accomplish the SPs classification task [35]. In addition, it can be jointly trained with the SSAE during fine-tuning of the parameters with labeled instances in a *supervised fashion*. The weight matrix θ is obtained by solving the convex optimization problem as following.

$$\arg\min_{\theta} J_s(\theta) = -\frac{1}{m}\sum_{i=1}^{m}\sum_{c=1}^{C}\mathbf{1}\{y_i = c\} \times \log P(y_i = c|x_i;\theta) + \frac{\lambda}{2}\|\theta\|_2^2 \qquad (5)$$

where $c \in \{1, C=2\}$ is the class label, $\widetilde{\mathrm{X}} = \{(x_1, y_1), (x_2, y_2), \ldots, (x_m, y_m),\}$ represents a set of labeled training instances, and the last term for the L_2 regularization.

Finally, fine-tuning was applied to boost the classification performance, and it treats all layers of the SSAE and the Softmax layer as a single model and improves all the weights of all layers in the network by using the backpropagation technique [35].

Hyper-parameters were not optimized explicitly but were determined via trial and error. Here are the final defined hyper-parameters (values) used in this study: maximum epochs of the SSAE (200), maximum epochs of the Softmax and fine-tuning (500), hidden layers size of the SSAE (100 and 50), sparsity parameter ρ (0.1), sparsity penalty β (5), L_2 regularization term λ for the SSAE and the Softmax (0.0001).

For evaluation of the AFS, we used leave-one-patient-out cross-validation (LOO CV) and reported the cross-validated accuracy, sensitivity, specificity, average area under the receiver operating characteristic (ROC) curve (AUC), and the Dice score.

3 Results and Discussion

In this study, we proposed a fully automatic framework for the AFS, which is based on the segmented anatomical structure of the LA and PVs using MA-WHS.

Fig. 1 (d) and (e) show the 3D MIP results overlaid on the segmented LA and PVs and LA wall and PVs boundaries overlaid on a LGE MRI slice respectively. The quantitative evaluations show that the MA-WHS based method achieved 0.90±0.12 Dice score, 9.53±6.01mm HD and 1.47±0.89mm ASD.

For the SSAE based SPs classification, we obtained LOO CV accuracy of 0.91, sensitivity of 0.95, specificity of 0.75, AUC of 0.95, and the Dice score for the final AFS was found to be 0.82±0.05.

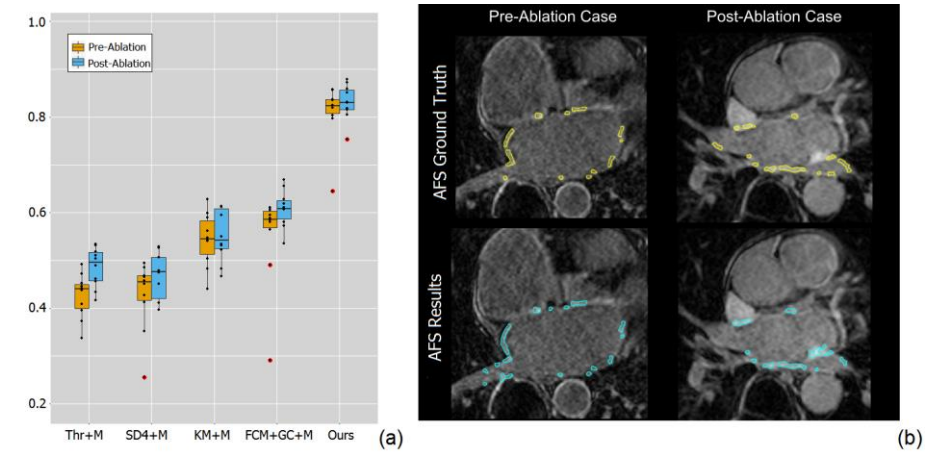

Fig. 2. (a) Boxplot for the comparison results of the Dice scores obtained by our fully automatic framework and other four methods (Thr, SD4, KM and FCM+GC) with manual delineated LA wall and PVs (+M); (b) Final AFS results (cyan regions) for an example pre-ablation (left) and an example post-ablation (right) case compared to the ground truth (yellow regions).

In addition, for the AFS, we compared our fully automatic framework with existing semi-automatic methods with manually delineated anatomical structure of the LA and PVs. The four methods we compared in this study were described in the benchmarking work [19], namely simple thresholding (Thr), conventional standard deviation (4 SDs were tested, i.e., SD4), k-means clustering (KM) and fuzzy c-means clustering with graph-cuts (FCM+GC). Fig. 2 (a) shows that our fully automatic framework obtained more accurate and more consistent results across 20 AF patient cases (Fig. 2 (a), red dots represent outliers), which can partly be attributed to the fact that our method is based on supervised learning. Of note is that, while in the benchmarking study these algorithms (i.e., Thr, SD4, KM and FCM+GC) were fine-tuned, in our comparison study, we have only implemented standard versions without performing further optimization. This is because details of the fine-tuning implemented for the benchmarking study are not available and in any case, that fine-tuning was done for datasets acquired in a different patient population to ours and may not be ideal. Despite this, similar performances were obtained between our implementation and those reported in [12] especially for the pre-ablation cases. For the post-ablation cases, our AFS results demonstrated similar results to the best-performing method reported in [12] but with smaller variance; however, our method has the advantage of being fully automatic. Of note is that multi-scanner and multi-institution datasets were used in the

benchmarking work and this may have resulted in a large variance in the images which could affect the final AFS segmentation. One of our future studies will be applying our fully automatic framework on multi-scanners LGE datasets to validate its robustness.

Fig. 2 (b) demonstrates that qualitatively our fully automatic AFS is in accordance with the manual segmented atrial fibrosis. However, if there are enhancements from the nearby mitral valve or blood pool regions, our method may mis-classify them as enhanced atrial fibrosis that is the major contribution for the false positives.

Another possible limitation of our study is that the SSAE based classifier has many hyper-parameters, which need to be carefully tuned, e.g., maximum epochs of the SSAE, maximum epochs of the Softmax and fine-tuning, hidden layers size of the SSAE, sparsity parameter ρ, sparsity penalty β, L_2 regularization term λ for the SSAE and the Softmax. Currently these hyper-parameters were tuned via trial and error, which may limit the final classification accuracy.

4 Conclusion

In conclusion, we have developed and validated a fully automatic framework to segment atrial fibrosis from LGE MRI images that is based on accurate anatomical structure delineation via a MA-WHS algorithm. The evaluation has been done on 20 LGE MRI scans for longstanding persistent AF patients that contain both pre-ablation and post-ablation cases. Based on the results, we can envisage a straightforward deployment of our framework for clinical usage. As a future direction, we will develop a more robust parameter tuning method for the applications on multi-scanners datasets.

References

1. Feinberg, W.M., Blackshear, J.L., Laupacis, A., Kronmal, R., Hart, R.G.: Prevalence, age distribution, and gender of patients with atrial fibrillation. Analysis and implications. Arch. Intern. Med. 155, 469–73 (1995).
2. January, C.T., Wann, L.S., Alpert, J.S., Calkins, H., Cigarroa, J.E., Cleveland, J.C., Conti, J.B., Ellinor, P.T., Ezekowitz, M.D., Field, M.E., Murray, K.T., Sacco, R.L., Stevenson, W.G., Tchou, P.J., Tracy, C.M., Yancy, C.W.: 2014 AHA/ACC/HRS Guideline for the Management of Patients With Atrial Fibrillation: Executive Summary. J. Am. Coll. Cardiol. 64, 2246–2280 (2014).
3. Pontecorboli, G., Figueras I Ventura, R.M., Carlosena, A., Benito, E., Prat-Gonzales, S., Padeletti, L., Mont, L.: Use of delayed-enhancement magnetic resonance imaging for fibrosis detection in the atria: a review. Europace. (2016).
4. Allessie, M.: Electrical, contractile and structural remodeling during atrial fibrillation. Cardiovasc. Res. 54, 230–246 (2002).
5. Boldt, A., Wetzel, U., Lauschke, J., Weigl, J., Gummert, J., Hindricks, G., Kottkamp, H., Dhein, S.: Fibrosis in left atrial tissue of patients with atrial

fibrillation with and without underlying mitral valve disease. Heart. 90, 400–405 (2004).
6. Haïssaguerre, M., Jaïs, P., Shah, D.C., Takahashi, A., Hocini, M., Quiniou, G., Garrigue, S., Le Mouroux, A., Le Métayer, P., Clémenty, J.: Spontaneous Initiation of Atrial Fibrillation by Ectopic Beats Originating in the Pulmonary Veins. N. Engl. J. Med. 339, 659–666 (1998).
7. Ravanelli, D., Dal Piaz, E.C., Centonze, M., Casagranda, G., Marini, M., Del Greco, M., Karim, R., Rhode, K., Valentini, A.: A novel skeleton based quantification and 3-D volumetric visualization of left atrium fibrosis using late gadolinium enhancement magnetic resonance imaging. IEEE Trans. Med. Imaging. 33, 566–576 (2014).
8. Fichtner, S., Sparn, K., Reents, T., Ammar, S., Semmler, V., Dillier, R., Buiatti, A., Kathan, S., Hessling, G., Deisenhofer, I.: Recurrence of paroxysmal atrial fibrillation after pulmonary vein isolation: is repeat pulmonary vein isolation enough? A prospective, randomized trial. Europace. 17, 1371–5 (2015).
9. Schmidt, E.J., Mallozzi, R.P., Thiagalingam, A., Holmvang, G., D'Avila, A., Guhde, R., Darrow, R., Slavin, G.S., Fung, M.M., Dando, J., Foley, L., Dumoulin, C.L., Reddy, V.Y.: Electroanatomic mapping and radiofrequency ablation of porcine left atria and atrioventricular nodes using magnetic resonance catheter tracking. Circ. Arrhythm. Electrophysiol. 2, 695–704 (2009).
10. Zhong, H., Lacomis, J.M., Schwartzman, D.: On the accuracy of CartoMerge for guiding posterior left atrial ablation in man. Heart Rhythm. 4, 595–602 (2007).
11. Peters, D.C., Wylie, J. V, Hauser, T.H., Kissinger, K. V, Botnar, R.M., Essebag, V., Josephson, M.E., Manning, W.J.: Detection of pulmonary vein and left atrial scar after catheter ablation with three-dimensional navigator-gated delayed enhancement MR imaging: initial experience. Radiology. 243, 690–695 (2007).
12. McGann, C.J., Kholmovski, E.G., Oakes, R.S., Blauer, J.J.E., Daccarett, M., Segerson, N., Airey, K.J., Akoum, N., Fish, E., Badger, T.J., DiBella, E.V.R., Parker, D., MacLeod, R.S., Marrouche, N.F.: New Magnetic Resonance Imaging-Based Method for Defining the Extent of Left Atrial Wall Injury After the Ablation of Atrial Fibrillation. J. Am. Coll. Cardiol. 52, 1263–1271 (2008).
13. Oakes, R.S., Badger, T.J., Kholmovski, E.G., Akoum, N., Burgon, N.S., Fish, E.N., Blauer, J.J.E., Rao, S.N., Dibella, E.V.R., Segerson, N.M., Daccarett, M., Windfelder, J., McGann, C.J., Parker, D., MacLeod, R.S., Marrouche, N.F.: Detection and quantification of left atrial structural remodeling with delayed-enhancement magnetic resonance imaging in patients with atrial fibrillation. Circulation. 119, 1758–1767 (2009).
14. Akkaya, M., Higuchi, K., Koopmann, M., Burgon, N., Erdogan, E., Damal, K., Kholmovski, E., McGann, C., Marrouche, N.F.: Relationship between left atrial tissue structural remodelling detected using late gadolinium

enhancement MRI and left ventricular hypertrophy in patients with atrial fibrillation. Europace. 15, 1725–1732 (2013).
15. Bisbal, F., Guiu, E., Cabanas-Grandío, P., Berruezo, A., Prat-Gonzalez, S., Vidal, B., Garrido, C., Andreu, D., Fernandez-Armenta, J., Tolosana, J.M., Arbelo, E., De Caralt, T.M., Perea, R.J., Brugada, J., Mont, L.: CMR-guided approach to localize and ablate gaps in repeat AF ablation procedure. JACC Cardiovasc. Imaging. 7, 653–663 (2014).
16. Badger, T.J., Daccarett, M., Akoum, N.W., Adjei-Poku, Y. a., Burgon, N.S., Haslam, T.S., Kalvaitis, S., Kuppahally, S., Vergara, G., McMullen, L., Anderson, P. a., Kholmovski, E., MacLeod, R.S., Marrouche, N.F.: Evaluation of left atrial lesions after initial and repeat atrial fibrillation ablation; Lessons learned from delayed-enhancement MRI in repeat ablation procedures. Circ. Arrhythmia Electrophysiol. 3, 249–259 (2010).
17. Arujuna, A., Karim, R., Zarinabad, N., Gill, J., Rhode, K., Schaeffter, T., Wright, M., Rinaldi, C.A., Cooklin, M., Razavi, R., O'Neill, M.D., Gill, J.S.: A randomized prospective mechanistic cardiac magnetic resonance study correlating catheter stability, late gadolinium enhancement and 3 year clinical outcomes in robotically assisted vs. standard catheter ablation. Europace. 17, 1241–50 (2015).
18. Perry, D., Morris, A., Burgon, N., McGann, C., MacLeod, R., Cates, J.: Automatic classification of scar tissue in late gadolinium enhancement cardiac MRI for the assessment of left-atrial wall injury after radiofrequency ablation. In: van Ginneken, B. and Novak, C.L. (eds.) In SPIE Medical Imaging. p. 83151D (2012).
19. Karim, R., Housden, R.J., Balasubramaniam, M., Chen, Z., Perry, D., Uddin, A., Al-Beyatti, Y., Palkhi, E., Acheampong, P., Obom, S., Hennemuth, A., Lu, Y., Bai, W., Shi, W., Gao, Y., Peitgen, H.-O., Radau, P., Razavi, R., Tannenbaum, A., Rueckert, D., Cates, J., Schaeffter, T., Peters, D., MacLeod, R., Rhode, K.: Evaluation of current algorithms for segmentation of scar tissue from late gadolinium enhancement cardiovascular magnetic resonance of the left atrium: an open-access grand challenge. J. Cardiovasc. Magn. Reson. 15, 105–122 (2013).
20. Knowles, B.R., Caulfield, D., Cooklin, M., Rinaldi, C.A., Gill, J., Bostock, J., Razavi, R., Schaeffter, T., Rhode, K.S.: 3-D visualization of acute RF ablation lesions using MRI for the simultaneous determination of the patterns of necrosis and edema. IEEE Trans. Biomed. Eng. 57, 1467–1475 (2010).
21. Karim, R., Arujuna, A., Housden, R.J., Gill, J., Cliffe, H., Matharu, K., Rinaldi, C. a, O'Neill, M., Rueckert, D., Razavi, R., Schaeffter, T., Rhode, K.: A Method to Standardize Quantification of Left Atrial Scar from Delayed-Enhancement MR Images. Transl. Eng. Heal. Med. IEEE J. 2, 1–15 (2014).
22. Tao, Q., Ipek, E.G., Shahzad, R., Berendsen, F.F., Nazarian, S., van der Geest, R.J.: Fully automatic segmentation of left atrium and pulmonary veins in late gadolinium-enhanced MRI: Towards objective atrial scar assessment. J. Magn. Reson. Imaging. 44, 346–354 (2016).
23. McGann, C., Akoum, N., Patel, A., Kholmovski, E., Revelo, P., Damal, K.,

Wilson, B., Cates, J., Harrison, A., Ranjan, R., Burgon, N.S., Greene, T., Kim, D., DiBella, E.V.R., Parker, D., MacLeod, R.S., Marrouche, N.F.: Atrial fibrillation ablation outcome is predicted by left atrial remodeling on MRI. Circ. Arrhythmia Electrophysiol. 7, 23–30 (2014).
24. Harrison, J.L., Sohns, C., Linton, N.W., Karim, R., Williams, S.E., Rhode, K.S., Gill, J., Cooklin, M., Rinaldi, C. a., Wright, M., Schaeffter, T., Razavi, R.S., O'Neill, M.D.: Repeat Left Atrial Catheter Ablation: Cardiac Magnetic Resonance Prediction of Endocardial Voltage and Gaps in Ablation Lesion Sets. Circ. Arrhythmia Electrophysiol. 8, 270–278 (2015).
25. Peters, D.C., Wylie, J. V., Hauser, T.H., Nezafat, R., Han, Y., Woo, J.J., Taclas, J., Kissinger, K. V., Goddu, B., Josephson, M.E., Manning, W.J.: Recurrence of Atrial Fibrillation Correlates With the Extent of Post-Procedural Late Gadolinium Enhancement. A Pilot Study. JACC Cardiovasc. Imaging. 2, 308–316 (2009).
26. Keegan, J., Jhooti, P., Babu-Narayan, S. V., Drivas, P., Ernst, S., Firmin, D.N.: Improved respiratory efficiency of 3D late gadolinium enhancement imaging using the continuously adaptive windowing strategy (CLAWS). Magn. Reson. Med. 71, 1064–1074 (2014).
27. Keegan, J., Drivas, P., Firmin, D.N.: Navigator artifact reduction in three-dimensional late gadolinium enhancement imaging of the atria. Magn. Reson. Med. 785, 779–785 (2013).
28. Zhuang, X., Shen, J.: Multi-scale patch and multi-modality atlases for whole heart segmentation of MRI. Med. Image Anal. 31, 77–87 (2016).
29. Tobon-Gomez, C., Geers, A., Peters, J., Weese, J., Pinto, K., Karim, R., Schaeffter, T., Razavi, R., Rhode, K.: Benchmark for algorithms segmenting the left atrium from 3D CT and MRI datasets. IEEE Trans. Med. Imaging. 34, 1460–1473 (2015).
30. Thévenaz, P., Unser, M.: Optimization of mutual information for multiresolution image registration. IEEE Trans. Image Process. 9, 2083–99 (2000).
31. Zhuang, X.: Challenges and methodologies of fully automatic whole heart segmentation: a review. J. Healthc. Eng. 4, 371–408 (2013).
32. Huttenlocher, D.P., Klanderman, G.A., Rucklidge, W.J.: Comparing images using the Hausdorff distance. IEEE Trans. Pattern Anal. Mach. Intell. 15, 850–863 (1993).
33. Xu, J., Luo, X., Wang, G., Gilmore, H., Madabhushi, A.: A Deep Convolutional Neural Network for segmenting and classifying epithelial and stromal regions in histopathological images. Neurocomputing. 191, 214–223 (2016).
34. Achanta, R., Shaji, A., Smith, K., Lucchi, A.: SLIC superpixels compared to state-of-the-art superpixel methods. IEEE Trans. Pattern Anal. Mach. Intell. 34, 2274–2281 (2012).
35. Hasan, M., Roy-Chowdhury, A.K.: A Continuous Learning Framework for Activity Recognition Using Deep Hybrid Feature Models. IEEE Trans. Multimed. 17, 1909–1922 (2015).